

Chapter 8

Fracture Interaction Behaviors



8.1 Introduction

Problems arising from hydraulic fracturing involve the nonlinear coupling of rock deformation and fluid flow, the nonlocal character of the fracture elastic response, the time dependence of fracture propagation and the interacting interference between the pre-existing and induced fractures. These problems will result in the offsetting of the fracture path and leak-off of fracturing fluid and then complicate the analysis of hydraulic fracturing [10]. Whereas the economic production from these reservoirs tends to depend on the efficiency of hydraulic fracturing stimulation treatment [26]. So fully modeling hydraulic fracturing is necessary and significant in optimizing the fracturing parameters and stimulating reservoir production.

Early research efforts concentrated on modeling the propagation of single planar hydraulic fracture (HF) in linear elastic, impermeable and homogeneous rock. As the horizontal in-situ stress in the overlying and underlying layers is much larger than that in the reservoir layer, the growth of HF height is expected to decline and ultimately stop, and therefore the phenomenon of constant fracture height appears [20, 30]. When the fracture length is sufficiently small compared to the fracture height, this hydraulic fracturing problem can be theoretically simplified to a plane-strain model, well-known as KGD and PKN models [11, 13, 18]. These models typically rely on the simplification of the fracturing problem either with respect to the fracture width profile or the fluid pressure distribution. However, the simple HF geometric assumption of a straight and bi-wing planar feature is untenable because of the pre-existing geological discontinuities including fissures, veins, joints, faults and bedding planes (assumed to be a natural fracture with a frictional interface and thereafter called NF) in naturally fractured formations [28]. The HF will inevitably intersect with multiple NFs and therefore result in complicated fracture networks [14]. Plenty of microseismic measurements and field observations [17, 9, 24] also suggest that the creation of complicated fracture networks is a common occurrence during the process of hydraulic fracturing treatments.

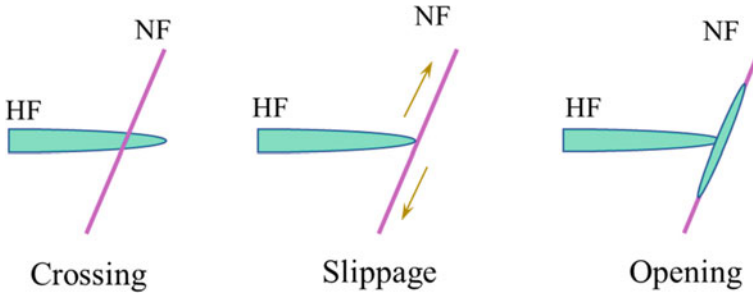


Fig. 8.1 Intersection modes between an HF and an NF [12]

Based on experiment and field analysis [4, 12, 33], three intersection modes (crossing, opening and slippage) were mainly observed when the HF propagated in naturally fractured formations as sketched in Fig. 8.1. The case of “Crossing”, “Opening” and “Slippage” means that the HF crosses the NF, the NF slips upon contact with HF, and the HF propagates along the dilated NF, respectively. The occurrence of each intersection behavior depends on the stress conditions and material mechanic properties to a large extent [22]. In reality, the minimum horizontal stress contrast defines the lower limit for the propagation capacity of the HF where the pressure for initiating a fracture needs to exceed the sum of the minimum horizontal stress and the rock tensile strength.

In this chapter, the goal is to predict the intersection behaviors (including crossing, slippage and opening) between the HF and the NF based on known parametric conditions and assumed geometric models. We pay attention to presenting a composite criterion to predict subsequent behaviors based on stress conditions before the HF comes into contact with the NF. This criterion is validated by comparing the predicted results with previously published experimental observations and intersection criteria. Furthermore, this new criterion includes the sensitivity of the HF approaching distance missed in previous intersection models, with which the new criterion is discussed in detail.

8.2 Intersection Model Between Hydraulic Fracture and Natural Fracture

As shown in Fig. 8.2a, a plane-strain model is developed considering a finite-length HF uniformly pressurized by internal fluid which is approaching an unbounded frictional NF (red rough line) at an arbitrary angle β . The internal fluid inside the HF is incompressible and inviscid. The initial stress field equals the far-field in-situ stress components σ_H and σ_h which are parallel and perpendicular to the HF in the Oxy reference plane, respectively. The yellow arrow denotes the injection location and

injection rate Q_0 . For convenience, a local coordinate system ($O' \beta x \beta y$) is established on the NF, where the βx axis is codirected with the NF in the direction of the approaching HF and intersects the βx axis at the NF midpoint (Fig. 8.2a).

During an HF approaching an NF, the stress components acting on the NF are influenced by the co-action of the fluid flow within the HF on both sides of the injection point and the far field in-situ stress. As the HF extends and moves closer to the NF, the stresses on NF increase and become closer to the critical failure thresholds (rock tensile strength or NF cohesion strength). Assuming a limit state where HF is infinitely close to but not in contact with the NF (Fig. 8.2b), the existing stress singularity near the HF tip will greatly influence the stress distribution on the NF, and certain points on the NF may have reached or even exceeded the critical failure limit. The possible behaviors of crossing, slippage and opening between the HF and the NF are assumed mutually independent. The mixed behaviors of opening after crossing and crossing after slippage are not considered.

8.2.1 Solution of Net Pressure Inside the Toughness-Dominated HF

Since the fracturing fluid is assumed to have zero viscosity, the propagation of HF can be identified be in the toughness-dominated regime [7]. The half-length of the HF is designated $l(t)$, the HF width is $w(x, t)$, P_{net} denotes the net pressure within the HF which only depends on the x coordinate (with origin at the injection point, O), and the fluid injection time is t .

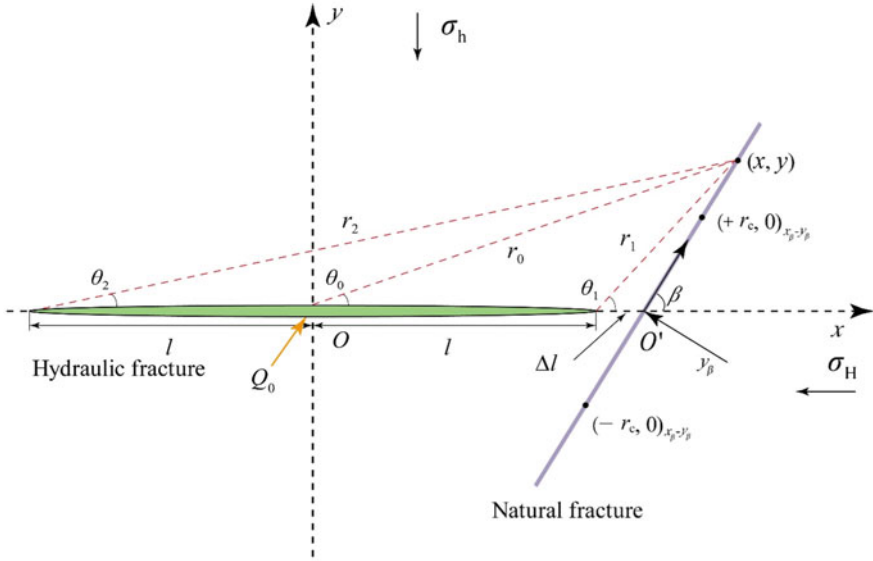
According to [7], the unified form of theoretical solution to a single fracture is defined in a dimensionless form:

$$\begin{aligned}
 l(t) &= L(t) \cdot \gamma[\rho(t)] \\
 w(x, t) &= \varepsilon(t) \cdot L(t) \cdot \Omega(\xi, t) \\
 P_{net}(x, t) &= \varepsilon(t) \cdot E' \cdot \Pi(\xi, t)
 \end{aligned}
 \tag{8.1}$$

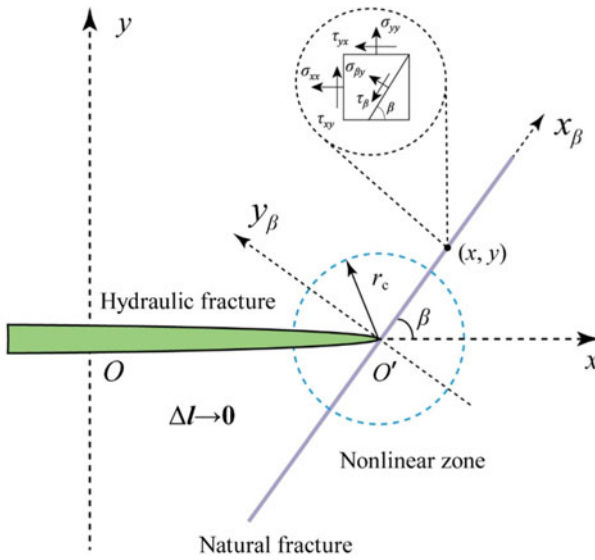
where $\xi = x/l(t)$ ($0 \leq \xi \leq 1$) refers to the scaled position which defines a moving system of coordinates (with respect to the fixed system of coordinates x); $\varepsilon(t)$ denotes a small dimensionless parameter that guarantees the variation range of Ω and Π from zero to infinity; L represents the length scale; γ , Ω , and Π are the dimensionless fracture half-length, opening and net pressure, respectively; and $\rho(t)$ is the dimensionless evolution parameter.

Based on the scaling of Eq. (8.1), the elasticity equation can be expressed as

$$\Omega = -\frac{4\gamma}{\pi} \int_0^1 \ln \left| \frac{\sqrt{1-\xi^2} + \sqrt{1-s^2}}{\sqrt{1-\xi^2} - \sqrt{1-s^2}} \right| \Pi(s, t) ds
 \tag{8.2}$$



(a) Geometry of the intersection model



(b) Limit state for $\Delta l \rightarrow 0$

Fig. 8.2 Schematic diagram of a hydraulic fracture approaching a natural fracture

The fluid lubrication equation can be written as

$$\left(\frac{\dot{\varepsilon}t}{\varepsilon} + \frac{\dot{L}t}{L}\right)\Omega - \frac{\dot{L}t}{L}\xi \frac{\partial \Omega}{\partial \xi} + \dot{\rho}t \left(\frac{\partial \Omega}{\partial \rho} - \frac{\xi}{\gamma} \frac{d\gamma}{d\rho} \frac{\partial \Omega}{\partial \xi}\right) = \frac{1}{G_m \gamma^2} \frac{\partial}{\partial \xi} \left(\Omega^3 \frac{\partial \Pi}{\partial \xi}\right) \quad (8.3)$$

The fluid mass balance is

$$2\gamma \int_0^1 \Omega d\xi = G_v \quad (8.4)$$

The HF propagation condition ($K_I = K_{IC}$) is

$$\Omega = G_k \gamma^{1/2} (1 - \xi)^{1/2}, \quad 1 - \xi \ll 1 \quad (8.5)$$

In the toughness-dominated regime, the dimensionless groups of G_v and G_k both equal 1, and G_m is a function expression about the known parameters ($G_m = \frac{\mu'}{\varepsilon^3 E' t}$, μ' represents the magnitude of fluid viscosity) according to [1]. The classic zero-viscosity solution of a toughness-dominated fracture is derived by Garagash [10], and the related dimensionless parameters are expressed as follows:

$$K' = \frac{8}{\sqrt{2\pi}} \cdot K_{IC}, \quad E' = \frac{E}{1 - \nu^2} \quad (8.6)$$

$$\varepsilon(t) = \left(\frac{K'^4}{E'^4 Q_0 t}\right)^{1/3}, \quad L(t) = \frac{E' Q_0 t^{2/3}}{K'} \quad (8.7)$$

$$\gamma = \frac{2}{\pi^{2/3}}, \quad \Omega(\xi) = \pi^{-1/3} \cdot (1 - \xi^2)^{1/2}, \quad \Pi = \frac{\pi^{1/3}}{8} \quad (8.8)$$

where E' is defined as plane-strain elastic modulus, ν denotes Poisson's ratio, K_{IC} is the rock fracture toughness and Q_0 represents the injection rate.

Finally, the hydraulic fracturing solution of a single HF is obtained by combining Eqs. (8.1) and (8.6) ~ (8.8):

$$l(t) = \gamma \cdot \left(\frac{E'}{K'}\right)^{2/3} \cdot (Q_0 t)^{2/3} \quad (8.9)$$

$$w(\xi, t) = \Omega(\xi) \cdot \left(\frac{K'}{E'}\right)^{2/3} \cdot (Q_0 t)^{1/3} \quad (8.10)$$

$$P_{\text{net}}(\xi, t) = E' \cdot \Pi(\xi) \cdot \left(\frac{K'}{E'}\right)^{4/3} \cdot (Q_0 t)^{-1/3} \quad (8.11)$$

8.2.2 Slippage Condition for the NF

The HF propagates is subject to the combined action of far-field in-situ stress (σ_H and σ_h) and inner fluid pressure (P_f). According to the stress superposition principle [23], the total stress on the NF interface should be equivalent to the superposition of the far field stress and the induced stress. The far field stress keeps uniform and is generated by in-situ stress, while the induced stress originates from the net pressure (P_{net}) within the HF and is generated by internal fluid flow.

According to Westergaard's analysis [27], the induced stress field produced by the net fluid pressure within the HF in Oxy reference plane is

$$\begin{cases} \sigma_{xx} = P_{net} \left[\frac{r_0}{2r^*} \right] \times \left[\begin{array}{l} 2 \cos(\theta^* - \theta_0) + 2 \sin \theta_0 \sin \theta^* - \sin \theta_1 \times \\ \sin(\theta^* + \theta_1 - \theta_0) - \sin \theta_2 \sin(\theta^* + \theta_2 - \theta_0) \end{array} \right] - P_{net} \\ \sigma_{yy} = P_{net} \left[\frac{r_0}{2r^*} \right] \times \left[\begin{array}{l} 2 \cos(\theta^* - \theta_0) - 2 \sin \theta_0 \sin \theta^* + \sin \theta_1 \times \\ \sin(\theta^* + \theta_1 - \theta_0) + \sin \theta_2 \sin(\theta^* + \theta_2 - \theta_0) \end{array} \right] \\ \tau_{xy} = P_{net} \left[\frac{r_0}{2r^*} \right] \times \left[\sin \theta_1 \cos(\theta^* + \theta_1 - \theta_0) - \sin \theta_2 \cos(\theta^* + \theta_2 - \theta_0) \right] \end{cases} \quad (8.12)$$

where

$$\begin{aligned} -\pi &\leq \{\theta_0, \theta_1, \theta_2, \theta^*\} \leq \pi, \\ r^* &= \sqrt{r_1 r_2}, & \theta^* &= \frac{1}{2} (\theta_1 + \theta_2), \\ r_0 &= \sqrt{x^2 + y^2}, & \theta_0 &= \tan^{-1} \left(\frac{y}{x} \right), \\ r_1 &= \sqrt{(x-l)^2 + y^2}, & \theta_1 &= \tan^{-1} \left(\frac{y}{x-l} \right), \\ r_2 &= \sqrt{(x+l)^2 + y^2}, & \theta_2 &= \tan^{-1} \left(\frac{y}{x+l} \right), \end{aligned}$$

The stress components of the HF-induced stress applied to the NF, inclined by the angle β with respect to the direction of σ_{xx} , are expressed as follows:

$$\begin{cases} \sigma_{P_{net}, \beta x} = \frac{\sigma_{xx} + \sigma_{yy}}{2} + \frac{\sigma_{xx} - \sigma_{yy}}{2} \cos(2\beta) + \tau_{xy} \sin(2\beta); \\ \sigma_{P_{net}, \beta y} = \frac{\sigma_{xx} + \sigma_{yy}}{2} - \frac{\sigma_{xx} - \sigma_{yy}}{2} \cos(2\beta) - \tau_{xy} \sin(2\beta); \\ \tau_{P_{net}, \beta} = -\frac{\sigma_{xx} - \sigma_{yy}}{2} \sin(2\beta) + \tau_{xy} \cos(2\beta); \end{cases} \quad (8.13)$$

The stress components projected on NF (inclined at angle β) from far-field stresses σ_H and σ_h are given by

$$\begin{cases} \sigma_{\gamma, \beta x} = \frac{\sigma_H + \sigma_h}{2} + \frac{\sigma_H - \sigma_h}{2} \cos 2\beta \\ \sigma_{\gamma, \beta y} = \frac{\sigma_H + \sigma_h}{2} - \frac{\sigma_H - \sigma_h}{2} \cos 2\beta \\ \tau_{\gamma, \beta} = -\frac{\sigma_H - \sigma_h}{2} \sin 2\beta \end{cases} \quad (8.14)$$

The total normal and shear stress of the combined stress field can be obtained by superposing Eqs. (8.5) and (8.6):

$$\begin{cases} \sigma_{\beta y} = \sigma_{P_{\text{net}}, \beta y} + \sigma_{\gamma, \beta y} \\ \tau_{\beta xy} = \tau_{P_{\text{net}}, \beta} + \tau_{\gamma, \beta} \end{cases} \quad (8.15)$$

When the normal stress on the NF is compressive, the failure of the interface can be judged by Mohr–Coulomb criterion (supposing compressive stress to be negative):

$$|\tau_{\beta xy}| \geq c - \mu \sigma_{\beta y} \quad (8.16)$$

where μ is the friction coefficient, c denotes the cohesion of the NF, $\sigma_{\beta y}$ and τ_{β} are the total normal and shear stresses on the NF interface, respectively.

The onset of slip is analytically estimated using the geometric model illustrated in Fig. 8.1b. If Eq. (8.16) holds, the NF may undergo shear failure at different degrees such that the growth of the HF will probably get arrested by the NF. Once the HF is arrested by NF, the pre-existing stress singularity at HF tip will diminish, and the stress field in the vicinity of the HF tip will differ significantly.

8.2.2.1 Opening Criterion for the NF

The critical fluid pressure required to open the NF and sustain the HF propagation [29] is

$$P_{\text{NF}} = \sigma_{\beta y} + \frac{K_{\text{IC}}}{\sqrt{\pi l}} \sqrt{\eta} \quad (8.17)$$

$$P_{\text{NF}} \leq P_{\text{HF}} \quad (8.18)$$

where $\eta = \gamma_{\text{NF}}/\gamma_{\text{Rock}}$, γ_{NF} and γ_{Rock} are the surface energy of the NF and the intact rock matrix, respectively.

The NF will be probably opened by the fracturing fluid inside the HF under the opening condition (Eq. 8.18) which defines the upper limit of the NF opening in combined stress field. Once the HF encounters the NF, the penetrating fracturing fluid may flow along either side of the NF midpoint, which highly depends on the intersection angle [21].

8.2.2.2 Crack Initiation Condition

According to the linear elastic fracture mechanics, the stress field near the fracture tip is approximated as

$$\begin{cases} \sigma_x = \sigma_H + \frac{K_I}{\sqrt{2\pi r}} \cos \frac{\theta}{2} \left(1 - \sin \frac{\theta}{2} \sin \frac{3\theta}{2}\right) \\ \sigma_y = \sigma_h + \frac{K_I}{\sqrt{2\pi r}} \cos \frac{\theta}{2} \left(1 + \sin \frac{\theta}{2} \sin \frac{3\theta}{2}\right) \\ \tau_{xy} = \frac{K_I}{\sqrt{2\pi r}} \sin \frac{\theta}{2} \cos \frac{\theta}{2} \cos \frac{3\theta}{2} \end{cases} \quad (8.19)$$

where K_I is the stress intensity factor, r and θ are the polar coordinates with the origin at HF tip, and $\theta = \beta$ (or $\beta - \pi$).

As the HF tip approaches the NF, the stress projected on the NF is increased such that the inelastic deformation is produced within a certain range of the HF tip, which implies the existence of a nonlinear region adjacent the approaching intersection point in limit state (Fig. 8.1b). Within the nonlinear region, the rock may stay in elastoplastic or plastic state and the highly accumulated elastic strain energy near the HF tip has been dissipated to some extent in the form of heat and surface energy, which makes the linear elastic fracture mechanics invalid for distances less than the critical radius (r_c) to the HF tip. Therefore, the effective stresses within nonlinear region is always assumed to be equal to or less than the stresses at r_c [2, 8, 12].

Similar to the notion of [12], which considered the inelastic behavior of the HF tip prior to contacting with the NF, the mechanical condition for a new fracture initiation on the opposite side of the NF interface is to achieve equilibrium between the maximum principle tensile stress and the rock tensile strength T_0 . Hence the critical initiating condition is given by

$$\sigma_1 = \frac{\sigma_x + \sigma_y}{2} + \sqrt{\left(\frac{\sigma_x - \sigma_y}{2}\right)^2 + \tau_{xy}^2} = T_0 \quad (8.20)$$

With known T_0 and K_{IC} (critical stress intensity factor), the nonlinear region critical radius r_c is derived by combining Eqs. (8.19) and (8.20).

Thus, the initiation position can be determined by checking the stress acting on the NF starting from the distance of r_c away from the NF midpoint. It follows then that crossing will occur if the stresses of certain points outside the nonlinear region ($r \geq r_c$) dissatisfy the shear failure condition (Eq. 8.16) and the opening condition (Eq. 8.18):

$$|\tau_{\beta xy}| < c - \mu \sigma_{\beta y}; \quad P_{NF} > P_{HF} \quad (8.21)$$

Many researchers [5, 25] have demonstrated that the in-situ stress difference and intersection angle were the predominant factors to be considered in the analysis of HF-NF intersection mechanism. Thus, we pay attention to the sensitivity of the stress difference of far-field maximum and minimum horizontal stresses and the intersection angle on the condition that other related parameters including fracture toughness, friction coefficient and initial fracture length remain constant.

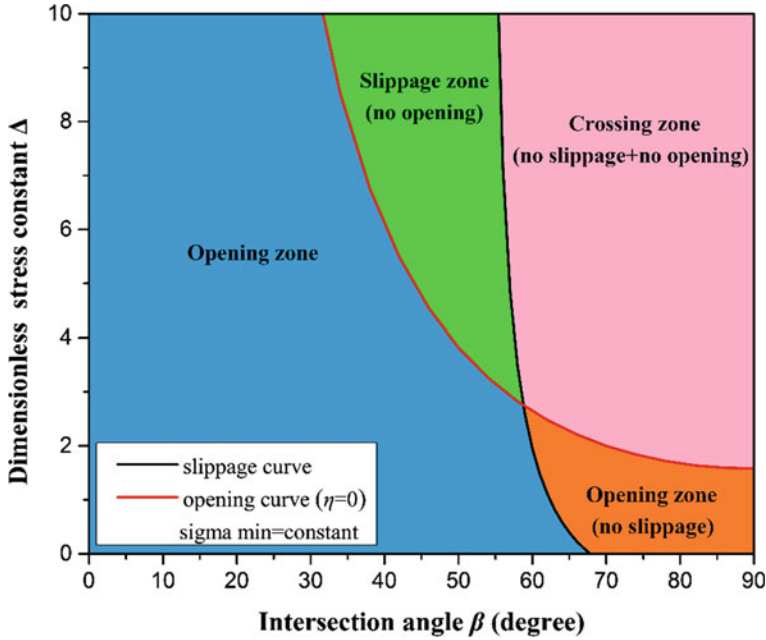


Fig. 8.3 Diagram of different intersection modes based on composite criterion where the dimensionless stress constant $\Delta = (\sigma_H - \sigma_h) / \sigma_h$

Combining the slippage, opening and initiation conditions expressed in Eqs. (8.16), (8.18) and (8.21), the possible intersection behaviors can be predicted mathematically with coded computational program, and the corresponding critical slippage as well as the opening curves can also be drawn out. As delineated in Fig. 8.3, the division of these zones is directly related to the critical shear failure condition and the critical opening condition of the NF. Therefore, the scope of each zone will also be directly related to the mechanical parameters of the two critical conditions.

8.3 Validation of Composite Criterion

8.3.1 Comparison with Previous Intersection Criteria

Previous research effort has concentrated on establishing effective predicting criterion for the HF-NF intersection behavior through theoretical and numerical analysis [4, 6, 15, 16, 25, 29]. To explore the discrepancy and advantage between the proposed criterion and previous criteria, we conduct a comparison using Blanton’s criterion, Gu and Weng criterion and Yao criteria under the same parametric conditions.

Figure 8.4 shows the boundary of different areas of the predicting intersection behavior corresponding to different analytical criteria in the parameter space of the intersection angles β and the horizontal in-situ stress difference. The initial material parameters are selected from Blanton experiments, where Devonian shale is chosen as the rock sample with tensile strength T_0 of 5.67 MPa (823 psi), fracture toughness K_{IC} of 1.59 MPa m^{1/2}, Young modulus E of 10 GPa and Poisson ratio ν of 0.22, NF cohesion c of 0 MPa, NF friction efficient μ of 0.75, minimum horizontal in-situ stress σ_h of 5 MPa (725 psi), initial HF length l of 0.06 m, and injection rate Q of 0.82e⁻⁶ m³/s.

(1) Blanton's criterion

In Blanton's experiments and analysis of HF-NF intersection [3] an intersection criterion was developed and validated through dynamic triaxial fracturing tests. The crossing will occur and the initiation of a new fracture can initiate provided that the treating pressure within the HF exceeds the superposition of the rock tensile strength and the stress acting parallel to the NF. After mathematical simplification, the final form of the crossing criterion is introduced by the following:

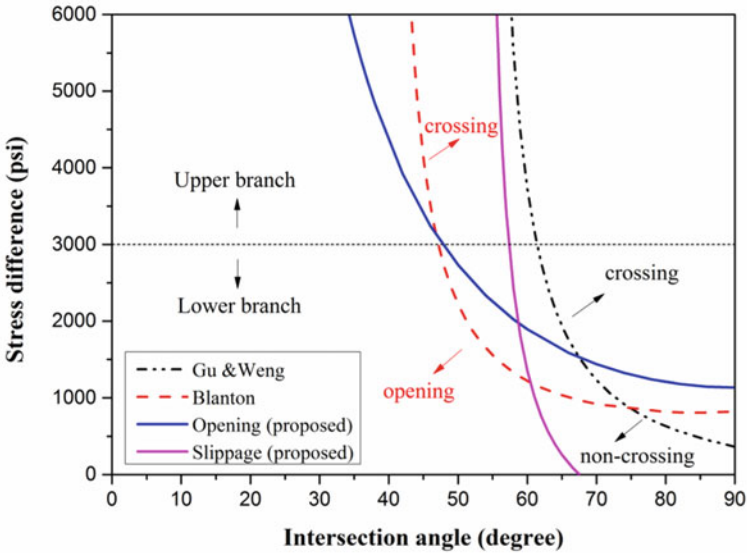
$$\sigma_H - \sigma_h > \frac{-T_0}{\cos 2\beta - b \sin 2\beta} \quad (8.22)$$

where $b = 0.2$ as an asymptote for an unbounded interface at the NF.

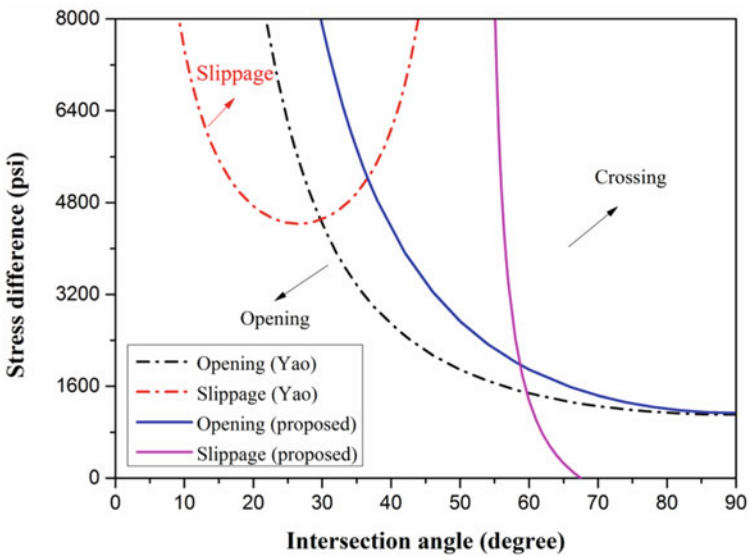
As shown in Fig. 8.4a (red dash line), the lower and upper branches of Blanton curve are almost parallel to the bottom segment of slippage curve and the top part of opening curve, respectively. This result implies that the two criteria have approximately identical predicting results for a relatively large and small intersection angle. However, based on the initial assumptions and mechanical conditions, the subsequent behavior predicted by Blanton criterion is either crossing or opening, but the case of slippage and the effect of induced stress field is not taken into consideration, which results in the criterion merely relating to three parameters (stress difference, intersection angle and b). Hence Blanton criterion is to some extent insufficient for predicting all of the intersection behaviors.

(2) Gu and Weng criterion (Gu and Weng criterion)

Gu et al. [12] considered an HF approaching a frictional interface prior to contact at non-orthogonal angles and proposed a crossing criterion based on linear elastic stress analysis near the fracture tip. This criterion can be applied to determine the occurrence of crossing provided that the accumulated fluid pressure is sufficient to initiate a new crack on the opposite side of the NF before the superposition stress consisting of the remote in-situ stress and the HF-tip stress field along the interface reaches the critical shear resistance. As shown in Fig. 8.4a (black dash-dot line), Gu and Weng criterion was plotted as the boundary between the area of crossing and no-crossing. And the crossing area is relatively reduced compared with the crossing region separated by the two critical curves of the composite criterion. As the intersection angle exceeds 67.5°, the lower branch of Gu & Weng crossing curve becomes closer to the x -axial



(a) Compared to Blanton and Gu & Weng criteria



(b) Compared to Yao criteria

Fig. 8.4 HF-NF criteria plotted as the boundary of the intersection areas

than that of the proposed opening curve but farther from the x -axial than that of the proposed slippage curve. These distinctions are attributable to the neglected effect of the inner fluid pressure inside the HF in Gu and Weng criterion.

Moreover, field and laboratory observations have demonstrated that opening is a common occurrence when investigating the intersection between the HF and NF [3, 5, 33]. The opening zone (no slippage) depicted in orange color in Fig. 8.3 also designates that the NF may also be dilated in the case of no slippage occurring, which will subsequently impede the HF propagation to penetrate across the NF.

(3) Yao criteria

In Yao's work [29], it is assumed that an HF gets blunted upon contacting an NF and will temporarily stay in the NF for a while and then breakout to propagate in a mechanically favorable direction depending on the orientation of natural fracture relative to the stress field. On basis of energy conservation and slip stability analysis, the opening and slippage criterion in terms of stress difference is derived and correspondingly expressed as:

$$\sigma_H - \sigma_h > \frac{K_{IC}(1 - \sqrt{\eta})}{\sqrt{\pi l} \sin^2 \beta} \quad (8.23)$$

$$\sigma_H - \sigma_h > \frac{c - \mu K_{IC}/\sqrt{\pi l}}{\sin \beta (\cos \beta - \mu \sin \beta)} \quad (8.24)$$

Yao criterion is delineated in Fig. 8.4b compared with the presented composite criterion. It can be seen that Yao's slippage curve is approximately manifested in the regulation of quadratic function, which means that the difficulty for slippage to occur decreases initially and then increases progressively with the increase of intersection angle. This significantly differs from the monotonically steep decrease of the slippage curve proposed herein. Furthermore, the opening curve of Yao outlines a larger crossing area than that of the composite criterion as the intersection angle decreases away from 90° .

8.3.2 Comparison with Laboratory Experiments

To validate the applicability of the composite prediction, the intersection behaviors predicted by current analytical model are compared to three independent laboratory experiments: Blanton experiments, Zhou experiments and Gu experiments [3, 4, 12, 33]. It should be noted that the value of η in Eq. (8.17) is assumed to be zero for the surface energy of NF is infinitely small compared with that of rock.

(1) Blanton experiments

Blanton [3] preformed the fracture intersection experiments using hydrostone blocks which were fractured by a pre-existing surface under different angles of approach

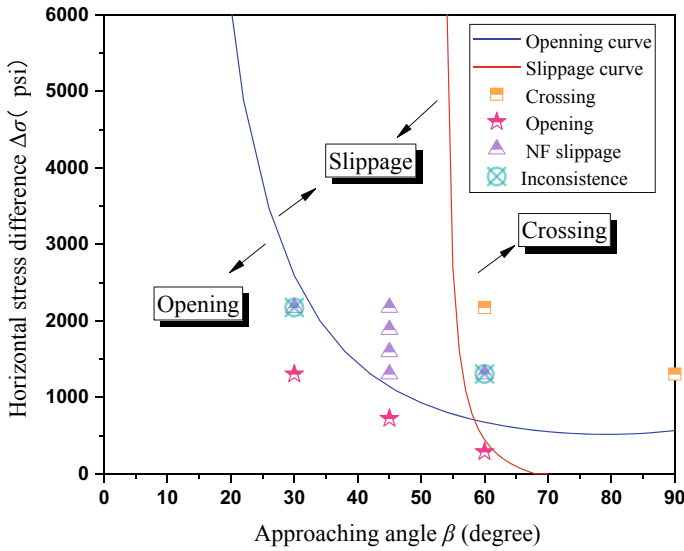


Fig. 8.5 Comparison between Blanton’s experimental results and predictions of the proposed composite criteria

(30°, 45°, 60° and 90°) and stress states ($-\sigma_h = 5$ or 10 MPa and the principal differential stresses varied from 2 to 15 MPa). The pre-fractured surface was frictional and cohesively with a friction coefficient of 0.75. The tensile strength of hydrostone was 3.1 MPa. And the Mode I fracture toughness was 0.176 MPa m^{1/2}. The fracturing fluid was injected at a constant flow rate of 0.82 cm³/s through a wellbore simulated by a steel pipe. In addition, the half-length of the HF was equal to 0.06 m. The fluid viscosity is assumed to be sufficiently small in a toughness-dominated HF, so its effect becomes negligible. Figure 8.5 summarizes the results of Blanton experiments and the corresponding calculation outcomes from the new criterion.

(2) Zhou experiments

Zhou et al. [33] reported similar experiments about the HF-NF intersection on cement-sand model blocks with scaled proportion to real rock in triaxial compressive stress state. The pre-fractures were created by 3 types of paper with cohesion of 3.2 MPa and friction coefficient of 0.38, 0.89 and 1.21, respectively. The interaction angles in each block between the HF and NF were varied systematically of 30°, 60° and 90°. The Mode I fracture toughness of model blocks is 0.59 MPa m^{1/2}, and the half-length of HF was designed as 0.06 m. The vertical stress remains invariable at 20 MPa, meanwhile, the horizontal stress difference was changed from 3 to 10 MPa. The comparison is shown in Fig. 8.6.

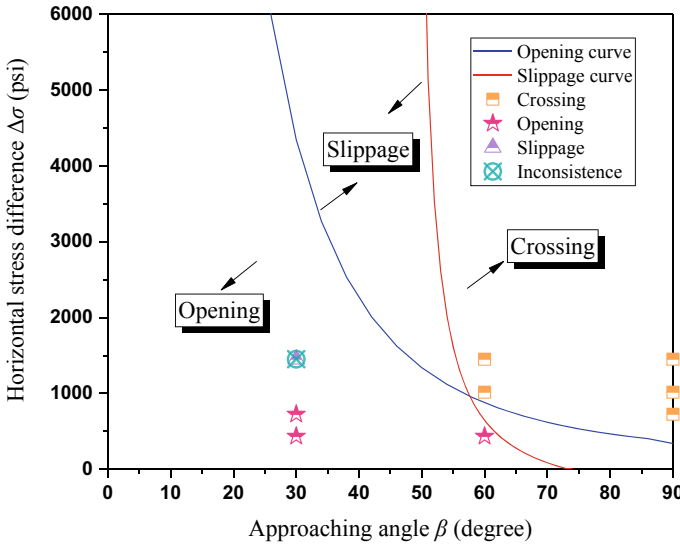


Fig. 8.6 Comparison between Zhou et al.’s experimental results and predictions of the proposed composite criteria

(3) Gu experiments

In recent experiments conducted by [12], Calton sandstone ($T_0 = 4.054$ MPa, $K_{IC} = 1.6$ MPa $m^{1/2}$) was cut into rectangle blocks and prepared for the intersection test at true triaxial-stress condition. A discontinuity interface characterized by friction efficient of 0.615 and negligible cohesion was prefabricated in the blocks at specified angles ranging from 45° to 90° . Silicone oil (viscosity of 1 Pa s) was injected at a constant rate of 0.5 cm^3/s . The vertical stress remains invariable at 27.58 MPa, meanwhile, the horizontal stress difference was changed from 0.69 to 10.35 MPa with unchangeable minimum horizontal stress of 6.89 MPa. And the initial half-length of HF was 0.076 m. The prediction results are depicted in Fig. 8.7.

In general, the comparison results in Figs. 8.5–8.7 indicate that the calculation outcomes obtained from the composite criterion show good agreement with the experimental results except for several particular cases. The disagreement between the experimental and predicted results arises from the inappropriate range of the nonlinear zone which implies that the actual nonlinear region at the crack tip is relatively larger. A possible explanation for this change is the co-action of stress singularity and plastic zone ahead of the HF tip which can enlarge the radius of the nonlinear zone. In this case, the initially calculated points at r_c no longer follow the linear elastic mechanics, resulting in inapplicable cases.

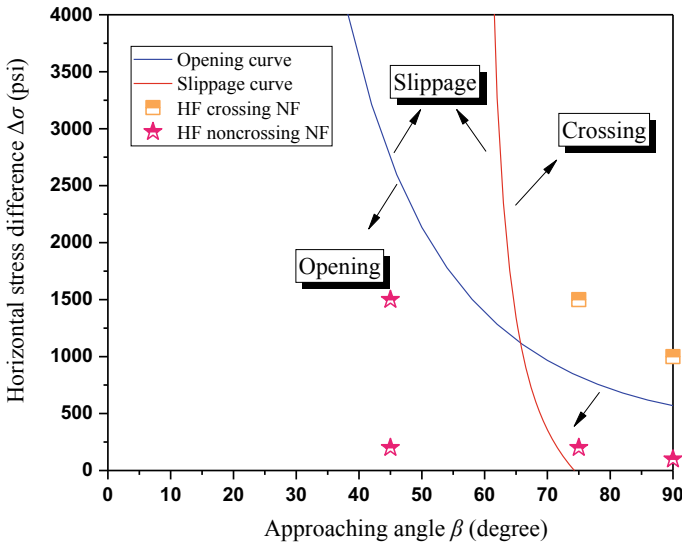


Fig. 8.7 Comparison between Gu et al.’s experimental results and predictions of the proposed composite criteria

8.4 Composite Criterion Considering Nonuniform Fluid Pressure

8.4.1 Nonuniform Form of Fluid Pressure

The intersection between a hydraulic fracture and a natural discontinuity is ubiquitous during hydraulic fracturing treatment. For better prediction of the fracture intersection, Zhao et al. [31, 32] proposed a composite criterion that synchronously considered three possible intersection modes (opening, crossing and arrested) and the coupling effects between fluid flow and solid elastic deformation. Nevertheless, the fluid effect in Zhao et al. [31, 32] is confined to a uniform pressure distribution at the limit intersection point where the hydraulic fracture is infinitely close to but does not intersect with the discontinuity. In this section, we aim to use the newly derived semianalytical solutions for the stress field induced by nonuniform fluid pressure and replace the induced stress field with that of constant fluid pressure. Subsequently, the induced stress is superimposed with far-field in-situ stress, and then the total stress field around the hydraulic fracture and possible fracture intersection can be evaluated. Meanwhile, we can compare the laboratory experimental observations of fracture intersection [25, 33] with the corresponding intersection results predicted by the semianalytical solution of nonuniform pressure, through which the validity and applicability of the presented semianalytical solution can be further demonstrated.

The specific polynomial form (Eq. (8.1)) was determined by fitting the analytical relationship of the nonuniform fluid pressure distribution along the crack referring to the first-order approximation of large toughness solutions in [7]. As depicted in Fig. 8.8, with the increase of the polynomial degree, the fitting precision (R -square) increases while the enlarged precision range decreases. Specifically, as the degree equals 7, it is easy to find that the continuous increase of the polynomial degree will only yield less than a 0.5% difference in accuracy. For convenience of calculation, we set the degree of fitting polynomial to 7. Then, referring to [1], the form of net fluid pressure inside the hydraulic fracture can be expressed as

$$P(x) = P_0\Pi = P_0\left(\frac{-137.128\xi^7 + 445.392\xi^6 - 567.697\xi^5 + 358.686\xi^4 - 116.684\xi^3 + 18.261\xi^2 - 1.249\xi + 0.373}{}\right) \tag{8.38}$$

where

$$P_0 = \left(\frac{K'^4}{E'Q_t}\right)^{1/3}, \quad \xi = x/a$$

$$K' = \frac{8}{\sqrt{2\pi}} \cdot K_{IC}, \quad E' = \frac{E}{1 - \nu^2}$$

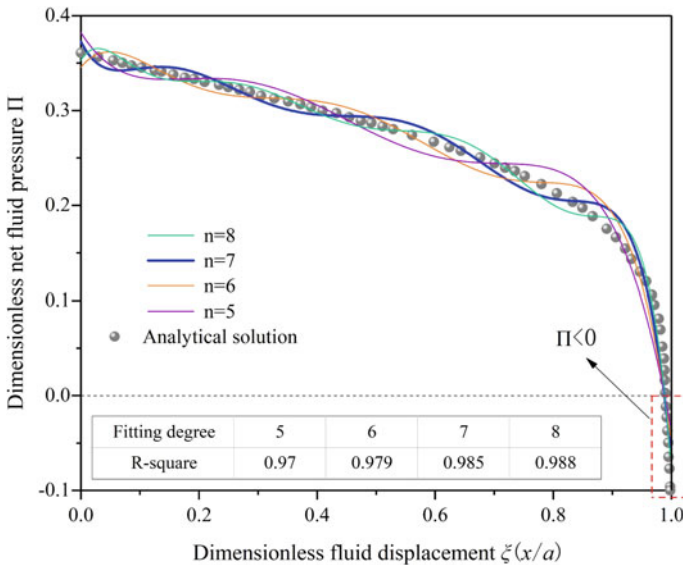


Fig. 8.8 Fitting curves of the non-uniform fluid pressure within a toughness-dominated crack based on [7]

It should also be noted that the net fluid pressure inside the crack is assumed to be always positive, but the abnormal negative Π marked in the red box near the region of $\xi = 1$ is attributed to the existence of stress singularity of the crack tip.

8.4.2 Comparison with Laboratory Experiments

Using this fitted pressure distribution as well as the critical conditions of the composite criterion presented by Zhao et al. [32], possible behaviors influenced by nonuniform fluid pressure under different in-situ stresses and approaching angles can be obtained. Meanwhile, the predicted results are also compared to previous conclusions, which neglected the effect of nonuniform fluid pressure in Zhao et al. [32].

Table 8.6 lists the results of Warpinski experiments [25], the corresponding calculation outcomes from the composite criterion of Zhao et al. [32] and the results predicted by the semianalytical solution for nonuniform fluid pressure. Note that the notation β refers to the intersection angle ($\leq 90^\circ$) between the hydraulic fracture and the natural discontinuity. The Warpinski experiment was deployed using Coconino sandstone (Young's modulus of 34.5 GPa, Poisson's ratio of 0.24, fracture toughness of $1.59 \text{ MPa m}^{1/2}$) that was processed into prismatic blocks and prepared for the intersection test under true triaxial stress conditions. A discontinuity interface characterized by a friction efficient (μ) of 0.68 and cohesion of 0.1 MPa was prefabricated at specified angles (β) ranging from 30° to 90° . Fracturing fluid was injected into the wellbore at a constant rate of $0.1 \text{ cm}^3/\text{s}$. The vertical stress was maintained at an invariable level for all tests, while the maximum horizontal in-situ stress (σ_H) changed from 6.89 to 13.79 MPa with an unchangeable minimum horizontal in-situ stress of 3.45 MPa. The initial half-length of HF was 0.06 m. In addition, the notation r_c denotes the critical radius of the plastic zone ahead of the fracture tip, and its corresponding calculation formula can be found in [19].

Table 8.7 shows the comparison of intersection results newly predicted by nonuniform fluid pressure with the Zhou experiment and the predicted outcomes of Zhao et al. [32]. In line with the experiment of Zhou [33], the model blocks were prepared from a mixture of No. 325 Chinese cement and fine sand with a tensile strength of 3.2 MPa, Young's modulus of 8.402 GPa and a Poisson's ratio of 0.23. Furthermore, a discontinuity interface characterized by three types of friction coefficients (0.38, 0.89, 1.21) and cohesion of 3.2 MPa was prefabricated in the blocks at specified angles (β) ranging systematically from 30° to 90° . The Mode I fracture toughness of the model blocks is $0.59 \text{ MPa m}^{1/2}$, and the half-length of hydraulic fracture was designated as 0.06 m. The injecting fluid is assumed to be incompressible, with a viscosity of 0.135 Pa s and an injection rate of $4.2 \times 10^{-9} \text{ m}^3/\text{s}$. The vertical stress remains invariable, and the maximum and minimum horizontal in-situ stress difference was changed from 3 to 10 MPa.

Tables 8.6 and 8.7 suggest that both constant and nonuniform fluid pressure can properly predict fracture intersection within a reasonable range of accuracy. However,

Table. 8.6 Comparison with Warpinski experiment and Zhao predicted results

β (°)	σ_H (MPa)	σ_h (MPa)	r_c (m)	μ	Experimental results	Constant predicted	Nonuniform predicted
30	6.89	3.45	0.0068	0.68	Opening	Opening	Opening
30	10.34	3.45	0.0067	0.68	Opening	Opening	Opening
30	13.79	3.45	0.0066	0.68	Arrested	Arrested	Arrested
60	6.89	3.45	0.0083	0.68	Opening	Arrested	Opening
60	10.34	3.45	0.0083	0.68	Crossing	Arrested	Crossing
60	13.79	3.45	0.0083	0.68	Crossing	Crossing	Crossing
90	6.89	3.45	0.0066	0.68	Opening	Crossing	Opening
90	10.34	3.45	0.0063	0.68	Crossing	Crossing	Crossing
90	13.79	3.45	0.0062	0.68	Crossing	Crossing	Crossing

Table. 8.7 Comparison with Zhou experiment and Zhao predicted results

β (°)	σ_H (MPa)	σ_h (MPa)	r_c (m)	μ	Experimental results	Constant predicted	Nonuniform predicted
90°	-8	-3	0.0020	0.38	Crossing	Crossing	Crossing
90°	-8	-5	0.0012	0.38	Crossing	Crossing	Crossing
60°	-10	-3	0.0026	0.38	Crossing	Crossing	Crossing
60°	-8	-3	0.0026	0.38	Opening	Crossing	Crossing
30°	-10	-3	0.0021	0.38	Arrested	Arrested	Arrested
30°	-8	-3	0.0021	0.38	Opening	Opening	Opening
90°	-10	-5	0.0011	0.89	Crossing	Crossing	Crossing
90°	-10	-3	0.0019	0.89	Crossing	Crossing	Crossing
60°	-10	-3	0.0026	0.89	Crossing	Crossing	Crossing
60°	-13	-3	0.0026	0.89	Crossing	Crossing	Crossing
60°	-8	-5	0.0026	0.89	Opening	Opening	Opening
30°	-10	-5	0.0012	0.89	Opening	Opening	Opening
30°	-8	-5	0.0012	0.89	Opening	Arrested	Opening
30°	-13	-3	0.0021	0.89	Arrested	Opening	Opening
90°	-8	-3	0.0020	1.21	Opening	Crossing	Crossing
90°	-13	-3	0.0019	1.21	Crossing	Crossing	Crossing
60°	-13	-3	0.0026	1.21	Opening	Crossing	Crossing
60°	-10	-3	0.0026	1.21	Opening	Crossing	Crossing
30°	-13	-3	0.0021	1.21	Opening	Opening	Opening
30°	-8	-3	0.0021	1.21	Opening	Opening	Opening

the difference is that the results using the semianalytical solution of nonuniform fluid pressure exhibited better agreement with the experimental observations than those predicted by Zhao et al. [32]. This distinction can be attributed to the variable fluid pressure inside the crack, which demonstrates the necessity to consider nonuniform fluid pressure. Furthermore, the fine matching between the experiments and the predicted results from nonuniform pressure further reveals the applicability of the presented semianalytical solutions for hydraulic fracturing analysis.

8.5 Perturbation Analysis of Key Parameters

The composite criterion is a function of horizontal in-situ stress, initial fracture length, intersection angle, fracture toughness and approaching distance. As mentioned above, the composite criterion curves of the stress difference versus the intersection angle were drawn and delineated at constant minimum horizontal stress and fracture toughness, and infinitesimally small approaching distance, which initially and geometrically restrict the composite criterion curve to be explored in depth. For further understanding fracture behavior at different parameters, it's necessary to conduct parametric sensitivity analysis considering minimum horizontal in-situ stress, fracture toughness and approaching distance, and conduct stress field analysis adjacent to the intersection. For convenience, a slip function f is introduced based on the slippage condition, which is expressed as:

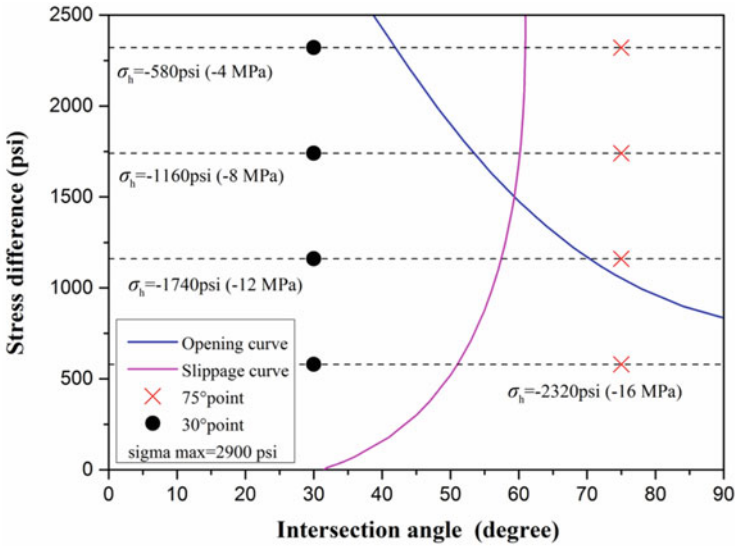
$$f = |\tau_{\beta xy}| - c + \mu\sigma_{\beta y}, \quad (\sigma_{\beta y} < 0) \quad (8.25)$$

Note that the increase of slip function means its absolute value decreases and the possibility of the NF slippage increases.

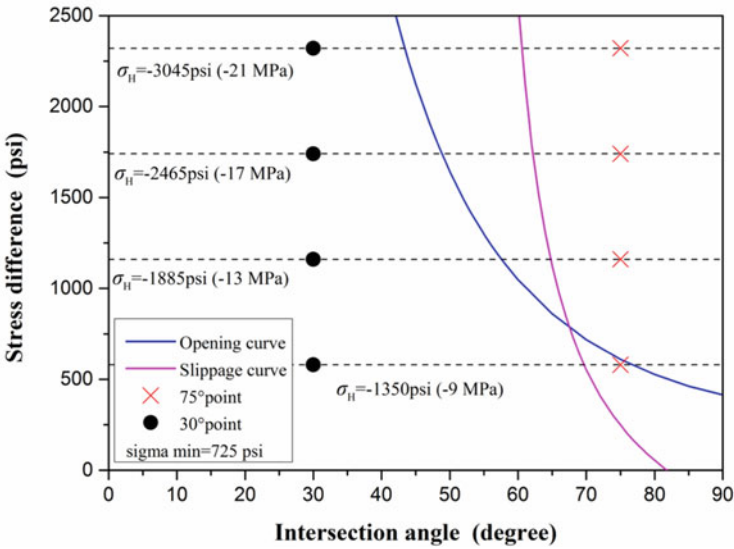
8.5.1 Impact of Initial Horizontal In-Situ Stress

The critical curves of the composite criterion considering the influence of varying the minimum horizontal stress at constant maximum horizontal stress and varying the maximum horizontal stress at constant minimum horizontal stress are depicted in Fig. 8.9a. To facilitate the contrast analysis, the critical curves of stress difference versus intersection angle at fixed minimum horizontal stress ($\sigma_h = -5$ MPa) are delineated in Fig. 8.9b. It should be specified that the critical curves in Fig. 8.9 are calculated and plotted at identical parametric conditions aside from initial value of the horizontal stress.

By comparison, it can be seen that as the variation of horizontal stress changes from decreasing σ_h to increasing σ_H , the slippage curve deflects symmetrically along the line $\beta = 60^\circ$ while the opening curve hardly exhibits significant changes in shape. On the other hand, there is an evident discrepancy in the curvature of opening curves in



(a) Composite criterion at constant maximum horizontal stress



(b) Composite criterion at constant minimum horizontal stress

Fig. 8.9 Influence of horizontal stress difference: **a** varying σ_h with fixed $\sigma_H = -20$ MPa (-2900 psi); **b** varying σ_H with fixed $\sigma_h = -5$ MPa (-725 psi)

Fig. 8.9a compared with Fig. 8.9b. The discrepancy mainly embodies in the decreased opening tendency and subsequently imposes greater difficulty for opening to occur. In addition, it's also easy to find that slippage becomes easier as the intersection angle β decreases from 90° according to Fig. 8.9a, which is opposite to the slipping tendency in Fig. 8.9b.

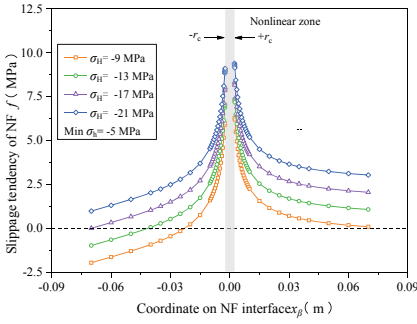
The slippage analysis of certain points at the intersection angle $\beta = 30^\circ$ (solid black dots) and $\beta = 75^\circ$ (red forks) with the stress difference of 4, 8, 12, 16 MPa are also respectively shown in Fig. 8.9. For further analysis of the NF stability, we solely concentrate on the slippage curves. We can predict that the solid black dots will probably slip whereas the red forks can remain stable regardless of the stress difference and initial horizontal stress value in line with their relative position to the slippage curves. This indicates that varying the minimum horizontal stress does not affect the final predicted intersection results at some intersection angles, thus it is feasible for the composite criterion to be used for the verification of the laboratory experiments as the minimum horizontal stress varies.

Figure 8.10 presents the slip function distribution on the NF interface when the HF approaches the NF at the angle of 30° (b) and 75° (c). Due to the existence of the stress singularity at the intersection, the starting points for calculation are determined by the radius of nonlinear region $\pm r_c$ and sixty points are symmetrically extracted from the natural frictional interface on both sides of the intersection in βx - βy coordinate system. The slip functions under different stress conditions share similar distribution characteristics of steep convex profile, which is manifested as the larger values of slip function for the closer distance to the intersection. And the slip function values of the calculation points on the negative NF interface ($\beta x < 0$) are less than those on positive NF interface ($\beta x > 0$). This difference means slippage is probably to occur on the positive NF rather than on the negative NF interface.

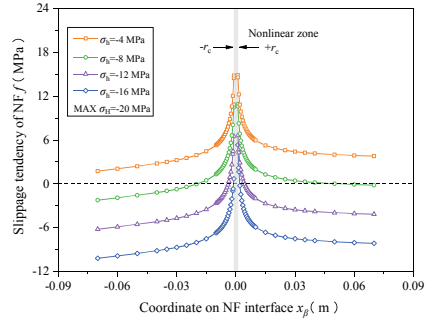
In addition, the values of slip function partially or entirely exceed zero for $\beta = 30^\circ$ in Fig. 8.10a, b, which implies the tangential stress applied along the NF is greater than the shear resistance and therefore further substantiates the slippage occurrence. As for $\beta = 75^\circ$, the values of slip function all stay below zero in spite of the initial horizontal stress (Fig. 8.10c, d). This result ensures sufficient stability to inhibit slippage on the NF interface. For clarity, the zero value of the slip function is marked out with dash lines shown in these figures.

8.5.2 Impact of Fracture Toughness

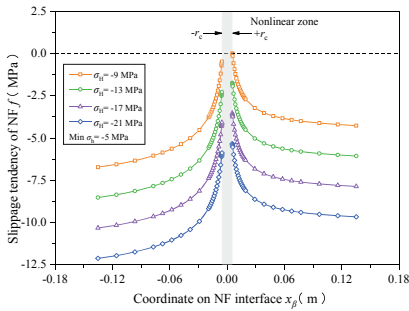
The opening and slippage curves of the composite criterion with fracture toughness of 0.59, 1.09, 1.59 and 2.09 MPa/m^{1/2} are plotted in Fig. 8.11. A small contrast in fracture toughness makes significant changes in the slippage curves whereas a relatively slight effect on the opening curve. Specifically, as the fracture toughness increases, the scope of crossing zone increases especially at low stress differences, while the slippage zone decreases despite the intersection angle and the stress difference. This



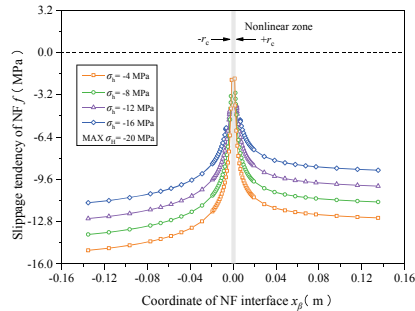
(a) Fixed σ_h and increasing σ_H ($\beta=30^\circ$)



(b) Fixed σ_H and increasing σ_h ($\beta=30^\circ$)



(c) Fixed σ_h and increasing σ_H ($\beta=75^\circ$)



(d) Fixed σ_H and increasing σ_h ($\beta=75^\circ$)

Fig. 8.10 Distribution of slippage tendency function f on the natural fracture interface

discrepancy signifies that the occurrence of crossing becomes easier at larger values of fracture toughness.

Furthermore, the opening curves have two-stage variation with the increase of fracture toughness: (i) distinguishable changes of the opening curves in the action of different fracture toughness are found in the angle range of $26\text{--}54^\circ$ (shadow area); (ii) the opening curves tend to coincide as the intersection angle increases from 54° . This allows us reach a conclusion that the effect of fracture toughness on the open curve is limited in a certain range of the intersection angle.

Figure 8.12 shows the slippage stability and stress distribution of the analyzed point. For different fracture toughness, the values of slip function of the analyzed point increase progressively as the calculated points move closer to the HF tip and finally presents a steep increase at the intersection. By comparison, the slip function on the positive βx axis is greater than that on the negative βx axis, indicating that the incipient slippage probably takes place on the right side of the NF rather than on the left. In general, the slip function increase with the increase of fracture toughness, which is contrary to the various laws in the coordinate interval of $(-0.14\text{ m}, -0.08\text{ m})$

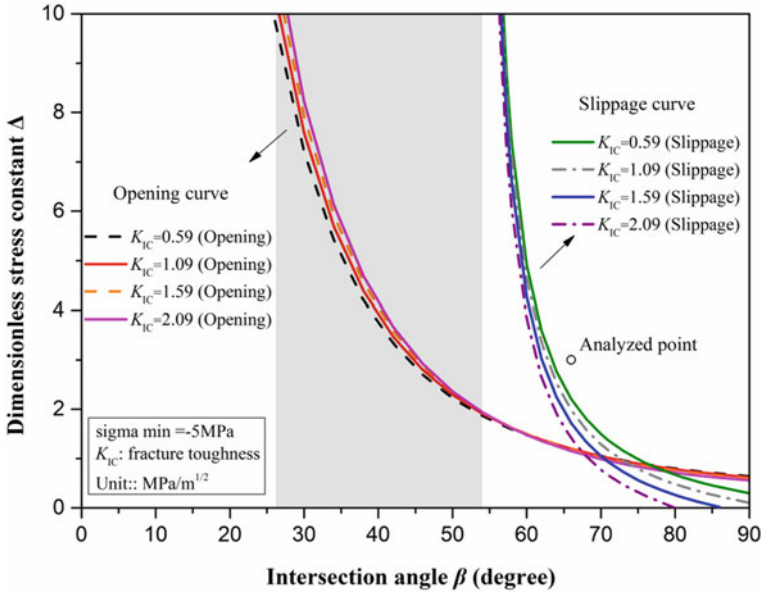
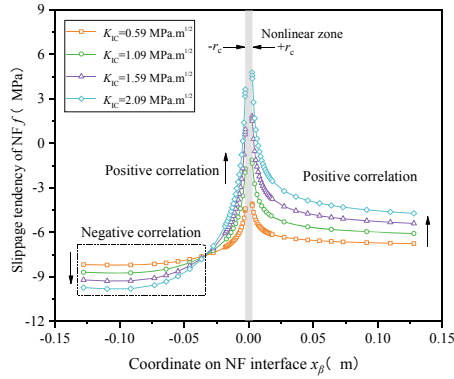


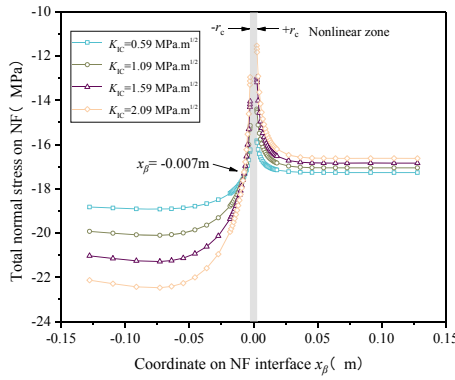
Fig. 8.11 Composite criteria considering the variation of rock fracture toughness

on the NF interface. Thus, the fracture toughness has a nonlinear effect on the slip function as the coordinate of the NF varies.

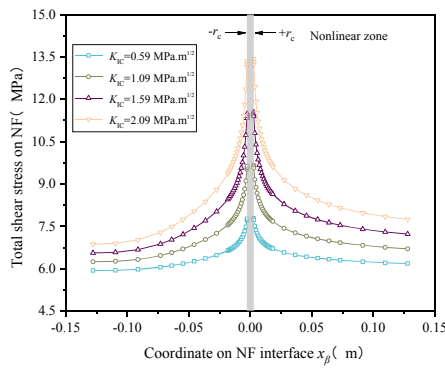
Moreover, the variation in the total normal stress with the increase of the fracture toughness on both sides of $\beta x = -0.02$ m is entirely contrary. The higher the fracture toughness gets, the smaller the total normal stress on the left side of $\beta x = -0.02$ m is, whereas the greater the normal stress on the right of $\beta x = -0.02$ m becomes. However, the contrast of the normal stress on the right of $\beta x = -0.02$ m is lower than that on the right side under different fracture toughness. A reasonable explanation for this result is that the calculated points at the positive βx axis are far from the HF, where the net pressure within the HF has an inappreciable stress component on the positive NF interface. As shown in Fig. 8.12c, the total shear stress appears approximately symmetrical distribution on both sides of the NF midpoint and has a positive correlation with fracture toughness. Hence the slippage stability of NF is mainly dominated by the total normal stress.



(a) Distribution of slippage tendency function on the natural fracture interface under different fracture toughness



(b) Total normal stress



(c) Total shear stress

Fig. 8.12 Slippage stability and stress distribution on the NF interface at analyzed point for intersection angle $\beta = 66^\circ$, $\sigma_H = -20 \text{ MPa}$ and $\sigma_h = -5 \text{ MPa}$

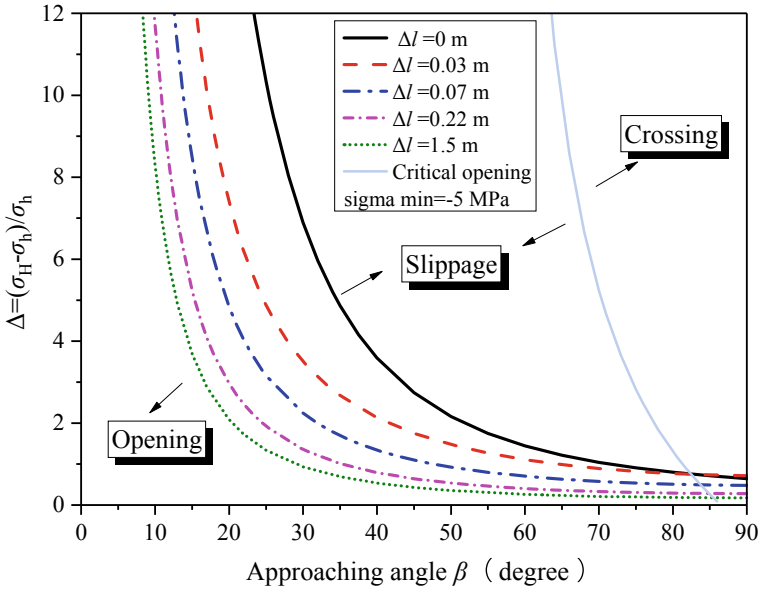
8.5.3 Impact of Approaching Distance

The approaching distance is introduced as a small perturbation between the right tip of HF and the intersection point, which aims to investigate whether the slippage will occur before the HF tip intersects with the NF. The magnitude of the approaching distance reflects the degree of HF tip close to the intersection. For the convenience of comparison, the HF half-length is assumed to be 6 m, and four sets of approaching distances (0, 0.03, 0.07, 0.22, and 1.5 m) are taken into account.

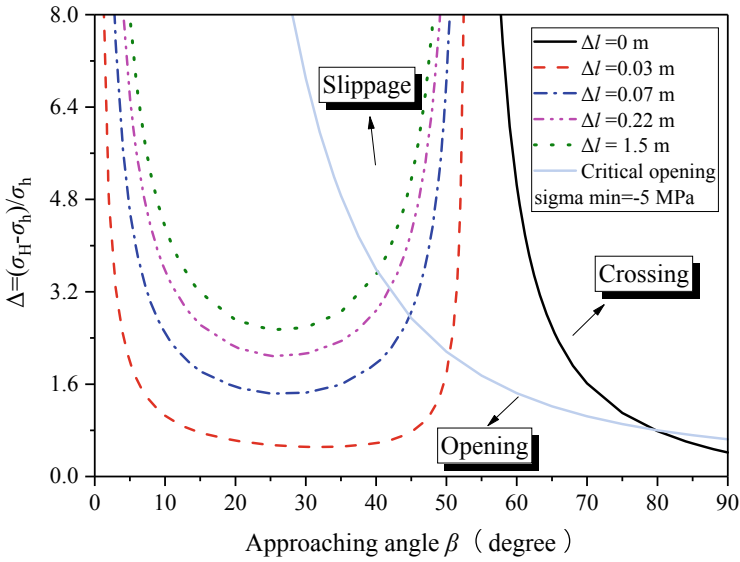
Figure 8.13 displays the critical opening and slippage curves under different approaching distances. With increasing approaching distance, the critical opening curves (Fig. 8.13a) are close to the coordinate axis, and the angle interval, within which the occurrence of the opening is more prone even at a relatively small stress difference, is surely reduced. Thus, it might become more difficult for the NF opening, especially at greater intersection angles. The opening can occur only under the prerequisite of the HF contacting HF. But here we merely concentrate on possible behaviors before the intersection. Thus, the opening curves are delineated by comparing the fluid pressure (P_{HF}) inside the HF with the total normal stress ($\sigma_{\beta y}$) acting perpendicularly to the NF, which defines the upper limit for opening to occur. In Fig. 8.13b, the larger value of approaching distance indicates the more symmetrical shape of the slippage curves. The form of asymmetrical curves for $\Delta l = 0.03$ m can be attributed to the combined action of fluid pressure and far-field in-situ stress. And as the approaching distance increases, the HF goes far away from the NF. So, the influence of fluid pressure diminished gradually and the remote in-situ stress starts to exert a dominating effect on the slippage.

The slip function curves in Fig. 8.14 show different tendencies under various intersection angles. In detail, the slip function curves are symmetrically distributed on both sides of the NF midpoint for $\beta = 90^\circ$. While β equals 60° , 30° and 10° , the values of slip function on the left side are greater than that on the right. This discrepancy is because the left side (negative βx axis) is closer to the HF than the right side, leading to a higher influence degree, which appears a larger variation magnitude of the slip function on the left.

In summary, the chance of slippage of the NF increases gradually during the approaching process. When the intersection angle increases from 30° to 90° , the slip function value decreases. And the natural fracture becomes less likely to slip, which indicates that the crossing behavior may more easily occur.



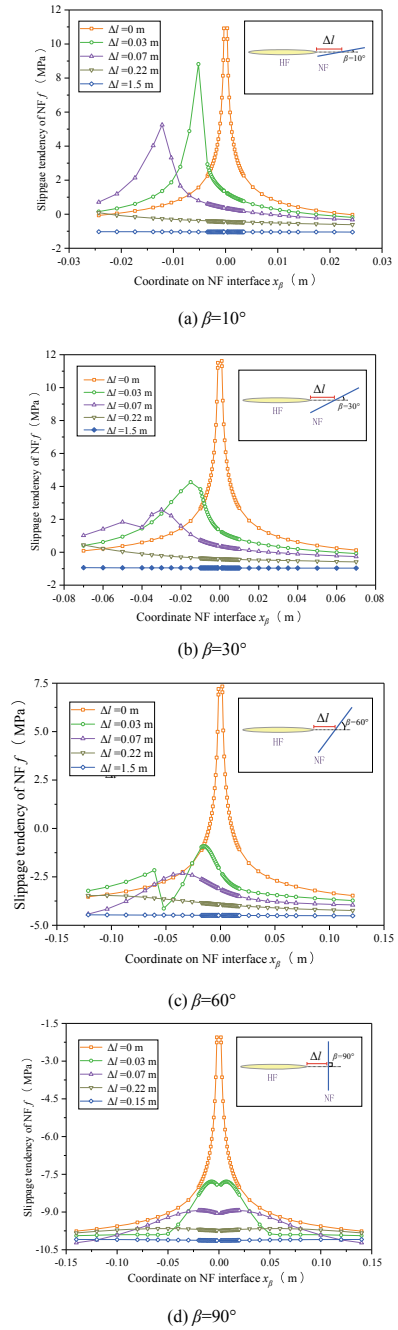
(a)



(b)

Fig. 8.13 The critical opening **a** and slippage **b** curves under different approaching distances ($\sigma_h = -5$ MPa)

Fig. 8.14 The slippage tendency (slip function) under different approaching distances for different intersection angles



References

1. Adachi JI (2001) Fluid-driven fracture in permeable rock. PhD thesis, Minneapolis University of Minnesota
2. Barenblatt GI (1962) The mathematical theory of equilibrium cracks in brittle fracture. *Adv Appl Mech* 7:55–129
3. Blanton TL (1982) An experimental study of interaction between hydraulically induced and pre-existing fractures. In: Society of petroleum engineers unconventional gas technology symposium, Pittsburgh. <https://doi.org/10.2523/10847-ms>
4. Blanton (1986) Propagation of hydraulically and dynamically induced fractures in naturally fractured reservoirs. In: SPE unconventional gas recovery symposium, society of petroleum engineers
5. Chuprakov D, Melchaeva O, Prioul R (2014) Injection-sensitive mechanics of hydraulic fracture interaction with discontinuities. *Rock Mech Rock Eng* 47(5):1625–1640
6. Dahi A, Olson JE (2011) Numerical modeling of multistranded-hydraulic-fracture propagation: accounting for the interaction between induced and natural fractures. *Soc Petrol Eng* 16:575–581. <https://doi.org/10.2118/124884-pa>
7. Detournay E (2004) Propagation regimes of fluid-driven fractures in impermeable rocks. *Int J Geomech* 4(1):35–45. [https://doi.org/10.1061/\(asce\)1532-3641\(2004\)4:1\(35\)](https://doi.org/10.1061/(asce)1532-3641(2004)4:1(35))
8. Dugdale DS (1960) Yielding of steel sheets containing slits. *J Mech Phys Solids* 8(2):100–104
9. Fisher MK, Davidson BM, Goodwin AK, Fielder EO, Buckler WS, Steinberger NP (2002) Integrating fracture mapping technologies to optimize stimulations in the barnett shale. In: Paper SPE 77411, SPE annual technical conference and exhibition, San Antonio, Texas, USA. <https://doi.org/10.2118/77441-ms>
10. Garagash (2000) Hydraulic fracture propagation in elastic rock with large toughness. In: Proceedings of 4th North American rock mechanics symposium, the Netherlands, 221–228
11. de Geertsma K (1969) A rapid method of predicting width and extent of hydraulic induced fractures. *J Petrol Technol* 21(12):1571–1581
12. Gu H, Weng X, Lund J, Mack M, Suarez-Rivera R (2011) Hydraulic fracture crossing natural fracture at non-orthogonal angles: a criterion and its validation. In: SPE hydraulic fracturing technology conference, society of petroleum engineers. <https://doi.org/10.2118/139984-pa>
13. Khrstianovic SA, Zheltov YP (1955) Formation of vertical fractures by means of highly viscous liquid. In: Proceedings of the fourth world petroleum congress, Rome, 579–586
14. Kresse O, Weng X, Wu R, Gu H. Numerical modeling of hydraulic fractures intersection in complex naturally fractured formations. *Am Rock Soc Assoc*. 2012. <https://doi.org/10.1007/s00603-018-1539-5>
15. Li ZC, Li LC, Li M et al (2018) A numerical investigation on the effects of rock brittleness on the hydraulic fractures in the shale reservoir[J]. *J Natl Gas Sci Eng* 50:22–32. <https://doi.org/10.1016/j.jngse.2017.09.013>
16. Liu HL, Li LC, Li ZC et al (2017) Numerical modelling of mining-induced inrushes from subjacent water conducting karst collapse columns in northern China[J]. *Mine Water Environ*. <https://doi.org/10.1007/s10230-017-0503-z>
17. Maxwell SC, Urbancic TI, Steinsberger NP, Zinno R (2002) Microseismic imaging of hydraulic fracture complexity in the Barnett shale. In: Paper SPE 77440, SPE annual technical conference and exhibition, San Antonio, Texas. <https://doi.org/10.2523/77440-ms>
18. Perkins T, Kern L (1961) Widths of hydraulic fractures. *J Pet Tech Trans AIME* 222:937–949
19. Renshaw CE, Pollard DD (1995) An experimentally verified criterion for propagation across unbounded frictional interfaces in brittle, linear elastic-materials. *Int J Rock Mech Mining Sci Geo-Mech Abstracts* 32(3):237–249
20. Sarmadivaleh M, Rasouli V (2013) Modified Renshaw and Pollard criteria for a non-orthogonal cohesive natural interface intersected by an induced fracture. *Rock Mech Rock Eng* 47(6):2107–2115
21. Song CP, Yiyu LU, Xia BW et al (2014) Effect of natural fractures on hydraulic fracture propagation in coal seam. *J Northeastern Univ (Natl Sci)* 35(5):756–760

22. Taleghani AD, Olson JE (2013) How natural fractures could affect hydraulic-fracture geometry. *SPE J* 19(1):161–171. <https://doi.org/10.2118/167608-pa>
23. Valko P, Economides MJ (1995) *Hydraulic fracture mechanics*. Wiley, Chichester
24. Warpinski NR, Kramm RC, Heinze JR, Waltman CK (2005) Comparison of single- and dual-array microseismic mapping techniques in the Barnett shale. In: Paper SPE 95568, SPE annual technical conference and exhibition, Dallas, Texas. <https://doi.org/10.2523/95568-ms>
25. Warpinski NR, Teufel LW (1987) Influence of geologic discontinuities on hydraulic fracture propagation. *J Petrol Technol* 39:209–220. <https://doi.org/10.2118/13224-Pa>
26. Xiaowei W (2015) Modeling of complex hydraulic fractures in naturally fractured formation. *J Unconventional Oil Gas Resour* 9:114–135
27. Westgaard HM (1939) Bearing pressures and crack. *J Appl Math Mech* 6:A49–A53
28. Wu R, Kresse O, Weng X, Cohen C-E, Gu H (2012) Modeling of intersection of hydraulic fractures in complex fracture networks. In: SPE hydraulic fracturing technology conference, Society of Petroleum Engineers. <https://doi.org/10.2118/152052-ms>
29. Yao, Y, Wang W, Keer LM. An energy based analytical method to predict the influence of natural fractures on hydraulic fracture propagation, *Engineering Fracture Mechanics*; 2017. <https://doi.org/10.1016/j.engfracmech.2017.11.020>.
30. Yew CH, Weng X (2014) *Mechanics of hydraulic fracturing*. Gulf Professional Publishing, Houston
31. Zhao Y, He PF, Zhang YF, Wang L (2019) A new criterion for a toughness-dominated hydraulic fracture crossing a natural frictional interface. *Rock Mech Rock Eng* 52:2617–2629. <https://doi.org/10.1007/s00603-018-1683-y>
32. Zhao Y, Yongfa Z, Pengfei H (2019) A composite criterion to predict subsequent intersection behavior between a hydraulic fracture and a natural fracture. *Eng Fract Mech* 209:61–78. <https://doi.org/10.1016/j.engfracmech.2019.01.015>
33. Zhou J, Chen M, Jin Y, Zhang GQ (2008) Analysis of fracture propagation behavior and fracture geometry using tri-axial fracturing system in naturally fractured reservoirs. *Int J Rock Mech Mining Sci Geo-Mech Abstracts* 45:1143–1152

Open Access This chapter is licensed under the terms of the Creative Commons Attribution 4.0 International License (<http://creativecommons.org/licenses/by/4.0/>), which permits use, sharing, adaptation, distribution and reproduction in any medium or format, as long as you give appropriate credit to the original author(s) and the source, provide a link to the Creative Commons license and indicate if changes were made.

The images or other third party material in this chapter are included in the chapter's Creative Commons license, unless indicated otherwise in a credit line to the material. If material is not included in the chapter's Creative Commons license and your intended use is not permitted by statutory regulation or exceeds the permitted use, you will need to obtain permission directly from the copyright holder.

